

Article

An Electronic Microsaccade Circuit with Charge-Balanced Stimulation and Flicker Vision Prevention for an Artificial Eyeball System

Yaogan Liang¹, Kohei Nakamura¹, Bang Du¹, Shengwei Wang¹, Bunta Inoue¹, Yuta Aruga¹, Hisashi Kino², Takafumi Fukushima¹, Koji Kiyoyama³ and Tetsu Tanaka^{1,2,*} 

¹ Graduate School of Engineering, Tohoku University, Sendai 980-8579, Japan

² Graduate School of Biomedical Engineering, Tohoku University, Sendai 980-8579, Japan

³ Graduate School of Engineering, Nagasaki Institute of Applied Science, Nagasaki 851-0193, Japan

* Correspondence: link@bc.mech.tohoku.ac.jp

Abstract: This paper presents the first circuit that enables microsaccade function in an artificial eyeball system. Currently, the artificial eyeball is receiving increasing development in vision restoration. The main challenge is that the human eye is born with microsaccade that helps refresh vision, avoiding perception fading while the gaze is fixed for a long period, and without microsaccade, high-quality vision restoration is difficult. The proposed electronic microsaccade (E- μ Saccade) circuit addresses the issue, and it is intrinsically safe because only charge-balanced stimulus pulses are allowed for stimulation. The E- μ Saccade circuit adopts light-to-frequency modulation; due to the circuit's leakage and dark current of light-sensitive elements, stimulus pulses of a frequency lower than tens of Hz occur, which is the cause of flickering vision. A flicker vision prevention (FVP) circuit is proposed to mitigate the issue. The proposed circuits are designed in a 0.18 μm standard CMOS process. The simulation and measurement results show that the E- μ Saccade circuit helps refresh the stimulation pattern and blocks the low-frequency output.

Keywords: artificial eye system; neural adaptation; electronic microsaccade; flicker vision prevention; charge-balancing stimulation



Citation: Liang, Y.; Nakamura, K.; Du, B.; Wang, S.; Inoue, B.; Aruga, Y.; Kino, H.; Fukushima, T.; Kiyoyama, K.; Tanaka, T. An Electronic Microsaccade Circuit with Charge-Balanced Stimulation and Flicker Vision Prevention for an Artificial Eyeball System. *Electronics* **2023**, *12*, 2836. <https://doi.org/10.3390/electronics12132836>

Academic Editors: Teen-Hang Meen, Chun-Yen Chang, Charles Tijus, Po-Lei Lee and Kuei-Shu Hsu

Received: 28 May 2023

Revised: 21 June 2023

Accepted: 24 June 2023

Published: 27 June 2023



Copyright: © 2023 by the authors. Licensee MDPI, Basel, Switzerland. This article is an open access article distributed under the terms and conditions of the Creative Commons Attribution (CC BY) license (<https://creativecommons.org/licenses/by/4.0/>).

1. Introduction

The ability to see is arguably humans primary information source. Millions of people worldwide suffer from eye diseases that can steal their vision, resulting in an increasing demand for vision restoration [1,2]. Individuals' quality of life (QoL) could be lowered significantly if any internal or external cause robs them of their vision. Unfortunately, age-related macular degeneration (AMD) and retinitis pigmentosa (RP), for example, can kill the photoreceptor cells in the human retina and finally lead to blindness. However, if the rest of the retinal cells are alive, vision restoration for patients with AMD and RP is possible by releasing electrical stimulation to the retinal nerve [3–5]. Other than AMD and RP, diabetic retinopathy, eye cancer, and severe glaucoma are also common causes of blindness. Hyperglycemia can destroy the capillaries and the layers of cells that support them in the retina, which is the cause of diabetic retinopathy [6]. High intraocular pressure in glaucoma can cause damage and the loss of ganglion cells [7]. Therefore, retinal prostheses become unavailable since no living cell exists for impulse generation and transmission.

Currently, artificial eyeballs show their strength in humanoid robots [8]. In the early days, vision restoration was demonstrated by connecting a television camera to a patient's visual cortex [9]. The previous work included a small computer, peripheral circuitry on a belt, and cables connecting with the patient's brain. Although vision perception was generated successfully, the drawback is the risk of infection and the high failure rate of the complex system [10]. Advanced CMOS technology allows imaging and stimulation

elements to be integrated into one chip, which makes a compact artificial vision system with high power efficiency possible. For powering the system, inductive links and photovoltaic cells are promising candidates [11–13]. Providing minor modifications, an artificial eyeball system mimicking the human eye can support vision restoration for virtually any blindness.

Figure 1 depicts an artificial eyeball system with an integrated image sensor and stimulator, which act as photoreceptor cells for light-to-nerve impulse conversion. In some previous studies, wireless power transfer was realized with the inductive coil, and a battery was expected to stabilize the power supply [11,14]. However, the human eye is born with an important ability, microsaccade, to prevent vision from fading [15–19]. In general, a strong neural response is generated in the biological eye when receiving rapid spatial and temporal brightness changes. With this feature, the human eye can efficiently detect subtle differences. The price to pay is that the still objects will fade away gradually due to neural adaptation. To counteract the issue, it is required to regularly refresh vision information.

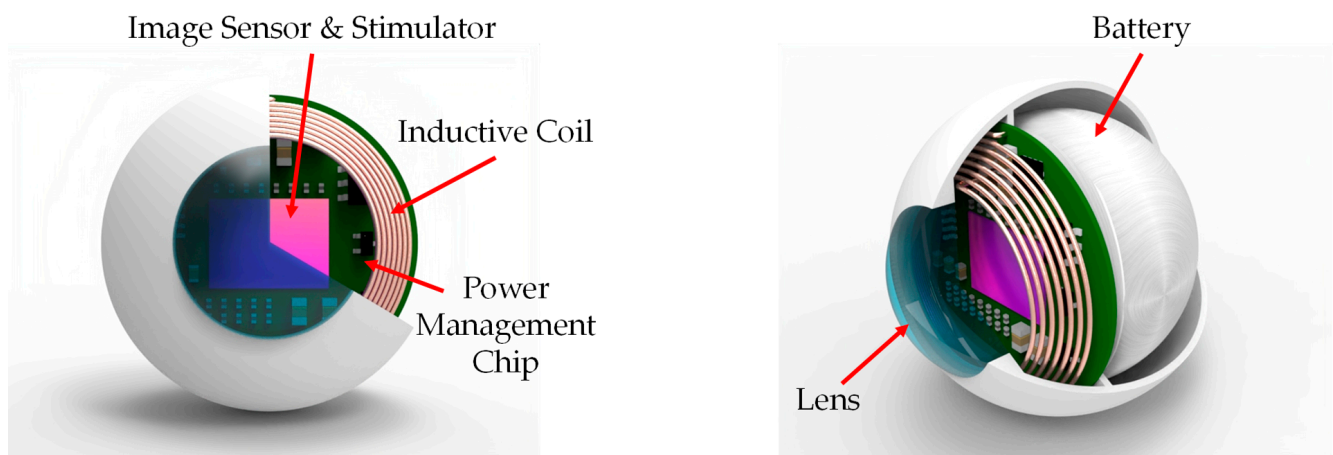


Figure 1. Concept images of artificial eyeball system for vision restoration.

Retinal prostheses are installed on the retina and share the eye’s movement, while the artificial eyeball has no connection with the eye muscle. Therefore, it has no vision refresh. Neural adaptation can arise when the gaze is fixed for a long period of time. For this reason, a weak response would be generated and finally fade away. Without addressing the issue, the user must constantly move the eyes for non-fading vision. In this work, the proposed approach adopts a customized circuit to regularly vary the vision information used for stimulation to alleviate vision fading. The details are included in Section 2.

As shown in Figure 2, because the charge balance of the stimulus current would be broken, a charge-balancing circuit is required for safe operation. In addition, low-frequency stimulus current can be generated because of transistor leakage and the photodiode’s dark current, resulting in flickering phosphenes [20–27]. This study is the first to propose the flicker vision prevention (FVP) circuit for dealing with the issue.

In this paper, we extend our previous work [28,29]. First, the methodology for designing the electronic microsaccade (E- μ Saccade) circuit is described. Next, charge-balancing and FVP circuits are presented. Section 3 shows the experimental results. Discussion and conclusions are in Sections 4 and 5, respectively.

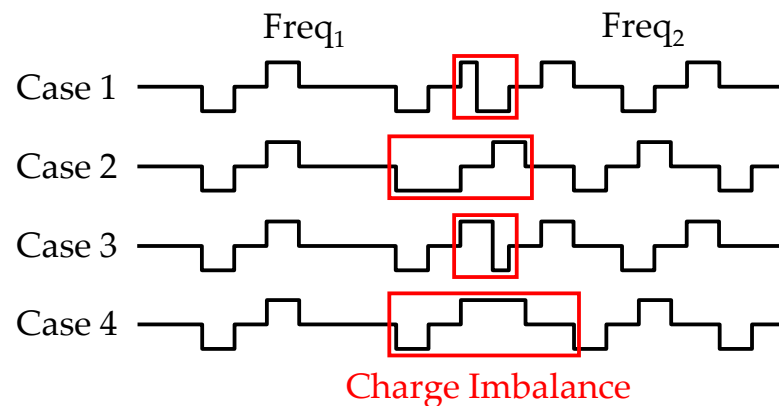


Figure 2. Charge imbalance in stimulus current.

2. Materials

2.1. Behavioral Model of Biological Eye

As depicted in Figure 3, the eyeball is constantly driven to move the gaze. The fixational eye movement, microsaccade, can prevent vision fading caused by neural adaptation [30]. In general, microsaccades show an amplitude of 1–120 arcmin and a frequency of 0.1–33 Hz [15]. The movement with 24 arcmin increases visibility most effectively, while the stimulus current with a frequency higher than 10 Hz is detrimental [31]. In our previous work, the pixel size of the retinal prosthesis was $75 \times 75 \mu\text{m}^2$, which can be translated into an angular separation of lines of 21.5 arcmin on the retina [28,32,33].

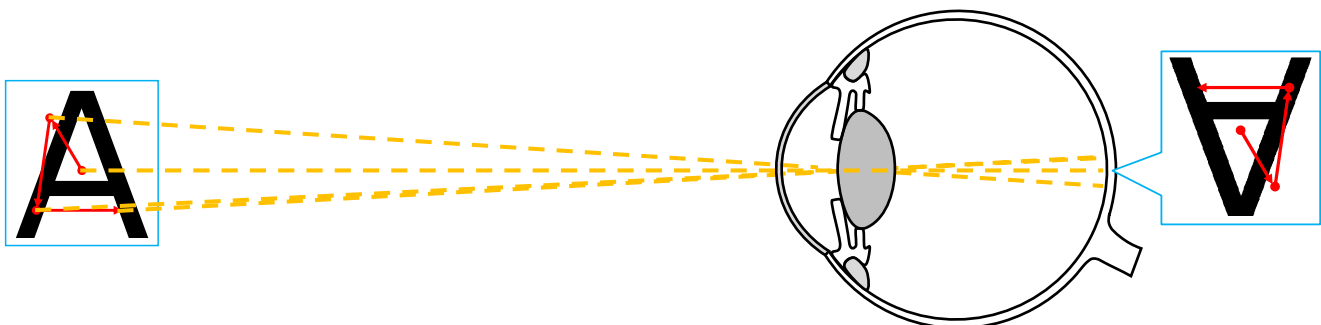


Figure 3. Microsaccade in the biological eye.

The cause of vision fading and the proposed solution when implanted with artificial eyeballs are shown in Figure 4a,b, respectively. The yellow circles represent electrodes being activated. When a fixed stimulus current pattern is applied to the neuron for a long period of time, the related neurons generate a gradually diminishing response and eventually stop action, like when the gaze is fixed. The issue becomes prominent as visually impaired patients usually interact with stationary objects. It has been reported that users of the artificial eye circuit must learn to recognize objects through a fading image [34].

Mathematically, the microsaccade acts the same as a slight movement of geometric figures. The operation can be translated as image convolution with a time-varying kernel, as shown in Figure 5. The kernel has only one non-zero element, and the value is always 1 (the black square). Applying the convolution to the retinal image can achieve image shifting, or microsaccade, in other words.

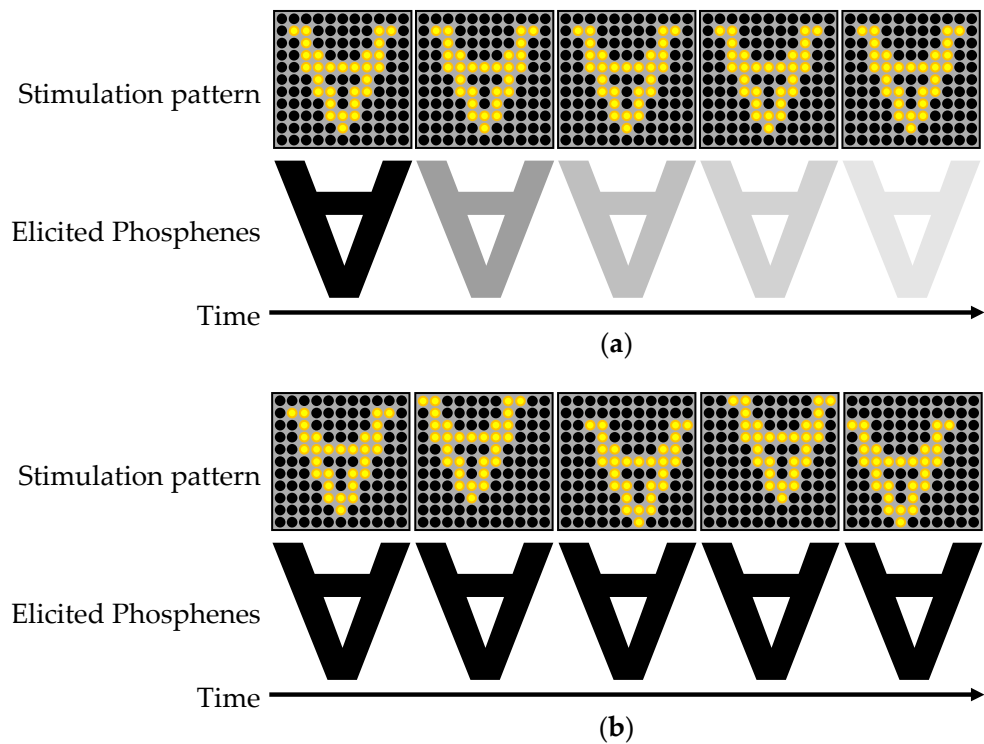


Figure 4. Operation of E-μSaccade circuit: (a) Stationary stimulation pattern causes vision fading; (b) Varying stimulation pattern helps to refresh visual perception.

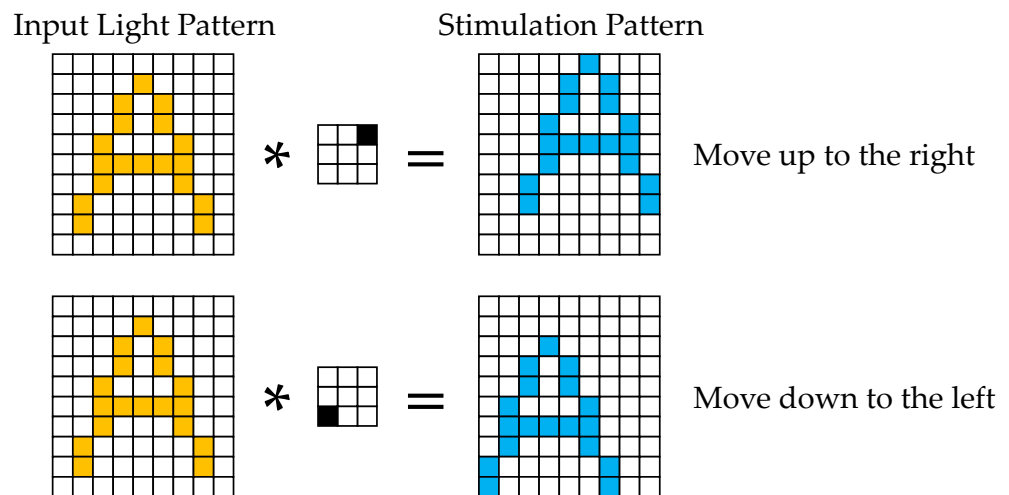


Figure 5. Principle of E-μSaccade circuit.

There are two possible solutions for generating fixational eye movement in the artificial eyeball: (1) vibrating the lens system to vary the light pattern; (2) electrically re-routing the signal from an image sensor pixel to a biphasic current source (BCS). The former requires motion elements, and the risk of mechanical failure is high. This work employs an electrical solution for better reliability. As shown in Figure 6, with the proposed E-μSaccade circuit, the stimulation pattern is moved slightly in random directions, like the microsaccade in the biological eye (Figure 3). The refresh rate is designed to be as close as possible to that of the biological eye so that the human brain can filter out the small image jitter. The elicited phosphenes are, therefore, stable and non-fading.

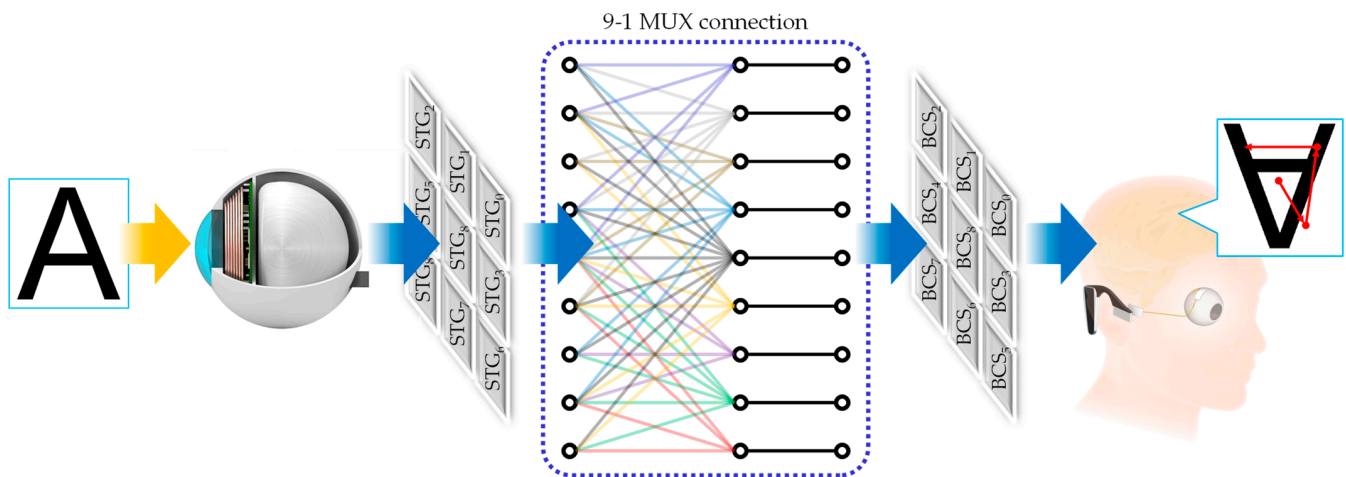


Figure 6. E- μ Saccade in the artificial eyeball.

The E- μ Saccade circuit connects nine adjacent stimulus trigger generators (STG) to one BCS and keeps the charge balanced during the circuit's operation. For activating vision neurons, the stimulus current depolarizes the cell membrane first and resets the membrane potential back to the resting potential [35]. The waveform parameters of stimulus current, such as pulse width and amplitude, must be designed elaborately to make the neurons respond to the stimulus current as maximally as possible. Since the E- μ Saccade circuit connects the image sensor pixel to different electrodes and all the pixels work asynchronously, there are risks of charge imbalance because the matching between anodic and cathodic pulses can be broken, as shown in Figure 2. Unbalanced stimulation would result in incorrect visual perception and damage to the nerve cells. In this work, the issue is mitigated by the proposed charge-balancing multiplexer (CBMUX). It improves the device's safety by making the anodic and cathodic pulses well-matched.

2.2. Implementation of Electronic Microsaccade Circuit

2.2.1. Light-to-Frequency Modulation

The STG is for light-to-frequency modulation. Its schematic is shown in Figure 7. Ambient light is converted into frequency-modulated VCT_{STG} and VAT_{STG} signals for triggering the BCS. In this work, a p-diffusion/n-well/p-sub structure photodiode is adopted for light sensing. In future development, the light-sensing element will be moved to an image sensor chip, and the STG will be in the stimulator chip. They can be connected through 3D-stacking technology. Following the photodiode, the current mirrors copy and amplify the photocurrent and then feed it to the modulation circuit. As shown in Figure 8 and described by Equations (1)–(5), the frequency of VCT_{STG} and VAT_{STG} signals is a function of photocurrent.

The timing diagram of STG is depicted in Figure 8. If the DIS_{STG} signal is 1, no stimulus current pulse appears on the output. The capacitor C_A determines the stimulus current's pulse repetition frequency (PRF). C_A is charged to the power rail after the reset phase. Then the photocurrent continuously discharges the C_A , and a Schmitt trigger monitors if V_A crosses the threshold voltage V_{SCH} . The RS latch in Figure 7 is for controlling the operation phase switching.

The pulse width of VCT_{STG} is given by Equation (3). In the beginning, the RS latch is in the initial state ($Q = 0$ and $QN = 1$), and when V_A reaches V_{SCH} , the AND gate outputs 1, turning on the current source I_B , and the cathodic pulse starts. After the Schmitt trigger flips to high, the capacitor C_B begins to be charged. The stored V_B is compared with the reference voltage V_{CW} , and the result is sent to the S terminal of the latch. If V_B crosses V_{CW} , the VCT_{STG} signal is stopped, and V_B is reset to 0 right after.

The above formulas calculate the key parameter of stimulus current. The PRF of the stimulus pulses is represented by f . T_{VCT} is the pulse width of the cathodic pulse, and T_{VAT} is the pulse width of the anodic pulse. T_{GAP} represents the interval between cathodic and anodic pulses, which helps to reduce the stimulation threshold [36–38]. T_{DIS} is the interval between two stimulation periods where no stimulus current appears. The threshold voltage of the Schmitt trigger is represented by V_{SCH} . The current flows into capacitors C_A , C_B , and C_C , which are represented by I_A , I_B , and I_C , respectively.

In the proposed circuit, to save space and achieve large capacitance, MIM capacitors are used. The process variation can result in circuit mismatches, lowering performance and reliability. Later, the effect will be described in Section 3.

2.2.2. Flicker Vision Prevention Circuit

Continuous vision perception is available when the PRF of the biphasic current is sufficiently high. The STG should not generate VCT_{STG} and VAT_{STG} signals whose frequency is lower than the perception threshold to avoid flickering vision. However, due to the transistor's leakage current and the photodiode's dark current, slow VCT_{STG} and VAT_{STG} signals are generated even without ambient light. For this reason, dark backgrounds or objects are represented by low-frequency stimulus pulses. The patients can perceive flickering patterns that correspond to the dark area. To improve image quality, the low-frequency stimulus current must be cut off.

The schematic of the FVP circuit is shown in Figure 9. It comprises AND gates, a timing capacitor C_D , and an RS latch. The electrode must be connected to the ground in the period between the cathodic and anodic pulses to release the residual charge on the cell membrane after the cathodic and anodic pairs are absorbed. The DIS_{STG} signal is high during these periods. A slow DIS_{STG} indicates a long stimulation period, and vice versa.

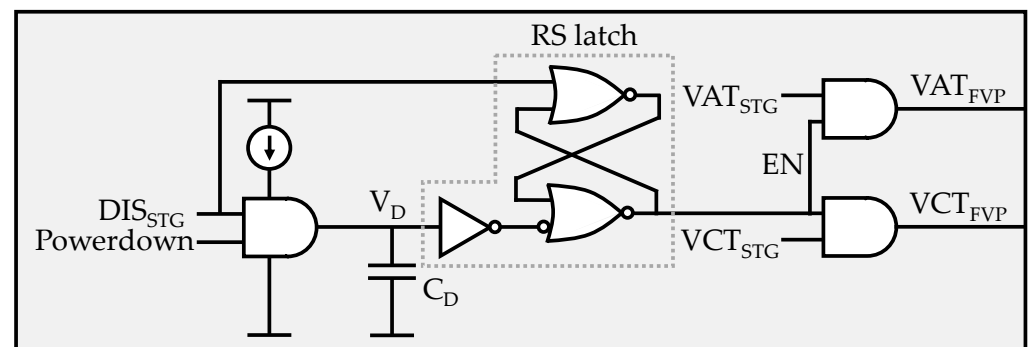


Figure 9. Schematic of flicker vision prevention (FVP) circuit.

The timing diagram of the FVP circuit is plotted in Figure 10. V_D ramps up when both the power down and DIS_{STG} are logically high. If EN is 1, VCT_{STG} and VAT_{STG} signals are allowed to pass through. With low illuminance conditions, the high level of DIS_{STG} lasts so long that V_D exceeds the threshold voltage of the latch and EN is set to low, stopping the stimulus pulse. When DIS_{STG} becomes low, the S terminal of the latch turns low instantly, and so does V_D . However, the R terminal remains high for a short period because of the additional delay. Therefore, EN is kept at 0, and all VCT_{STG} and VAT_{STG} pulses are blocked. EN is reset to high when a rising edge of the DIS_{STG} signal occurs. The FVP circuit enters the next operation period. With higher stimulation frequencies, because DIS_{STG} is short and V_D does not cross the trigger threshold, EN stays at 1, allowing pulses to pass through.

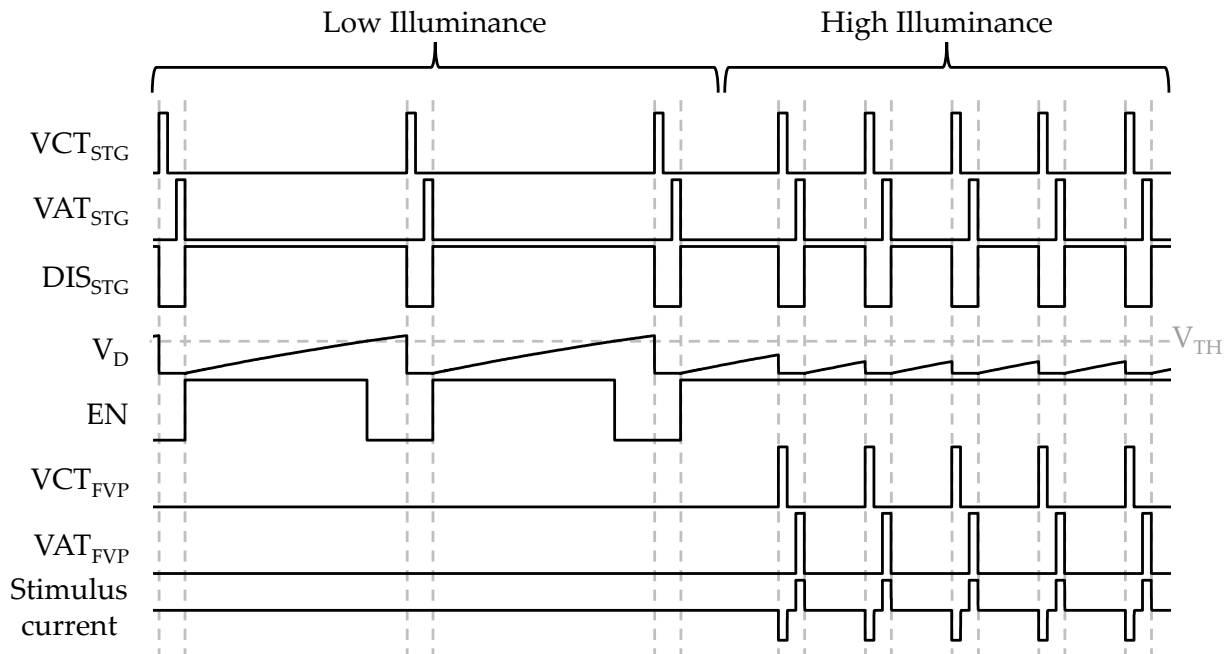


Figure 10. Timing diagram of flicker vision prevention circuit.

2.2.3. Charge-Balancing Multiplexer for Safe Electronic Microsaccade

The core component of the E- μ Saccade circuit is the CBMUX; the schematic is depicted in Figure 11. In the CBMUX, the 9-channel MUX selects VCT and VAT signals according to the pixel selection code (PSC). The definition of PSC is listed in Table 1. DFF1 receives an external clock signal, CLK_{MS} , and DFF2 controls the phase switching. DFF3 generates a DIS_O signal for residual charge release during two stimulation periods. For charge balancing, DFF4 and DFF5 count the VCT_I pulses and change the circuit state properly. Then stimulus trigger signals VAT_O and VCT_O are generated after two rising edges of the VCT_I . For not breaking the matched pulses, a latch is used to save PSC temporarily.

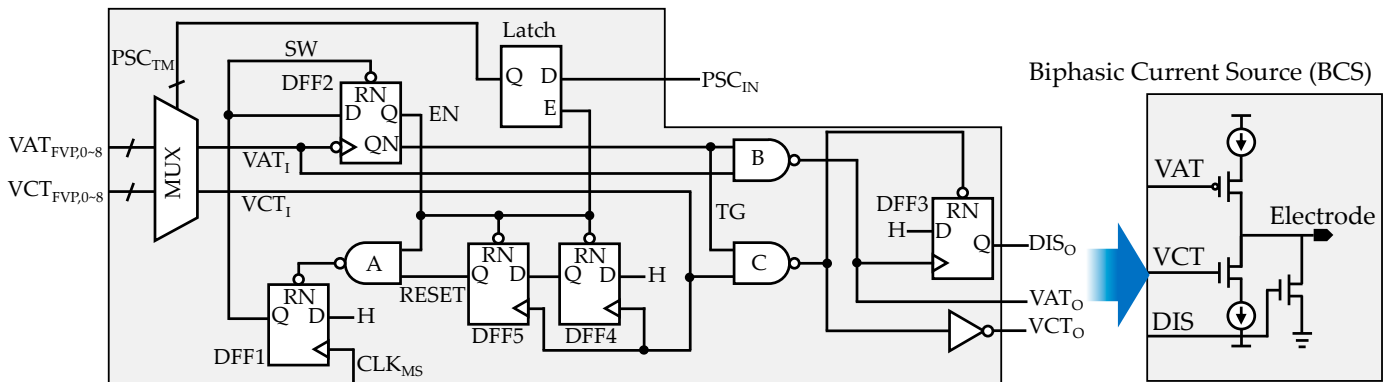


Figure 11. Schematic of charge-balancing multiplexer (CBMUX).

The timing diagram of CBMUX is shown in Figure 12. For simplicity, only two related channels, $VCT_{FVP,1-2}$ and $VAT_{FVP,1-2}$, are demonstrated. The CLK_{MS} signal controls circuit-state switching. Before t_2 , there is no clock signal. $VCT_{FVP,1}$ and $VAT_{FVP,1}$ pass through CBMUX to VCT_O and VAT_O . Then, CLK_{MS} rises at t_2 , indicating that a switching event occurs. At the same time, a PSC is fed to the CBMUX. The switching event is recorded by setting the SW signal to 1. VCT_O and VAT_O follow $VCT_{FVP,1}$ and $VAT_{FVP,1}$ because the latch holds the previous PSC. At t_4 , a stimulation period is completed. The latch is enabled because EN is high, and the new PSC is sent to the MUX. Then the MUX selects $VCT_{FVP,2}$

and VAT_{FVP2} . Meanwhile, TG is pulled low, stopping the stimulus-triggered pulses. No pulse is allowed between t_4 and t_5 . To not break down the charge balance, two DFFs are used for counting the VCT_I signal. When VCT_I triggers the circuit reset procedure at t_5 , the circuit is reset to the initial state ($SW = 0$, $EN = 0$, $TG = 1$). With this mechanism, the anodic and cathodic pulses are well matched.

Table 1. True table of charge-balancing multiplexer.

PSC (BCD Code)	Signal Path from STG to BSC
0	VAT and VCT from the upper-left STG
1	VAT and VCT from the upper-center STG
2	VAT and VCT the upper-right STG
3	VAT and VCT from the middle-left STG
4	VAT and VCT from the middle-right STG
5	VAT and VCT from the lower-left STG
6	VAT and VCT from the lower-center STG
7	VAT and VCT from the lower-right STG
8	VAT and VCT from the central STG
≥ 9	N/A

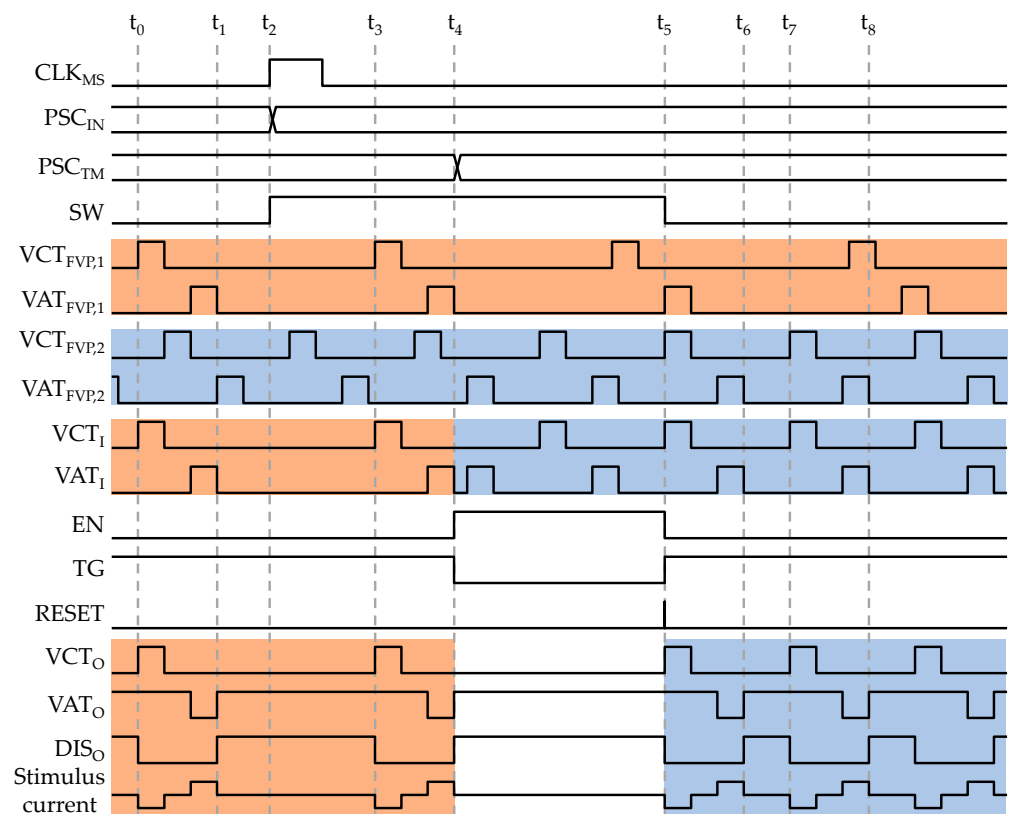


Figure 12. Timing diagram of charge-balance multiplexer.

3. Results

Circuit simulation is conducted for functional verification. The photodiode in STG is replaced with a current source, and a resistor of 10 kΩ is added to the electrode terminal of BCS as a tissue load. First, the FVP circuit is turned off to verify the time-domain response of STG. A current step is applied to the STG. Due to the fact that incident light is attenuated in the eyeball when reaching the retina, the STG is designed to work with low illuminance. The current steps are from 1 pA to 100 pA at 0 s. Figure 13a shows the frequency step of the stimulus current, and the input current step is plotted. The corresponding waveform of stimulus current (converted into voltage with a 10 kΩ resistor) is plotted in Figure 13b. The

results report that the STG can correctly track the rapid change of incident light. Figure 13c depicts the frequency variation of stimulus current when photocurrent ramps from 1 pA at 0 s to 100 pA at 1 s. Despite some nonlinear distortion, STG gives a satisfactory result in tracking the ramp change of the photocurrent. The corresponding time-domain waveform is shown in Figure 13d.

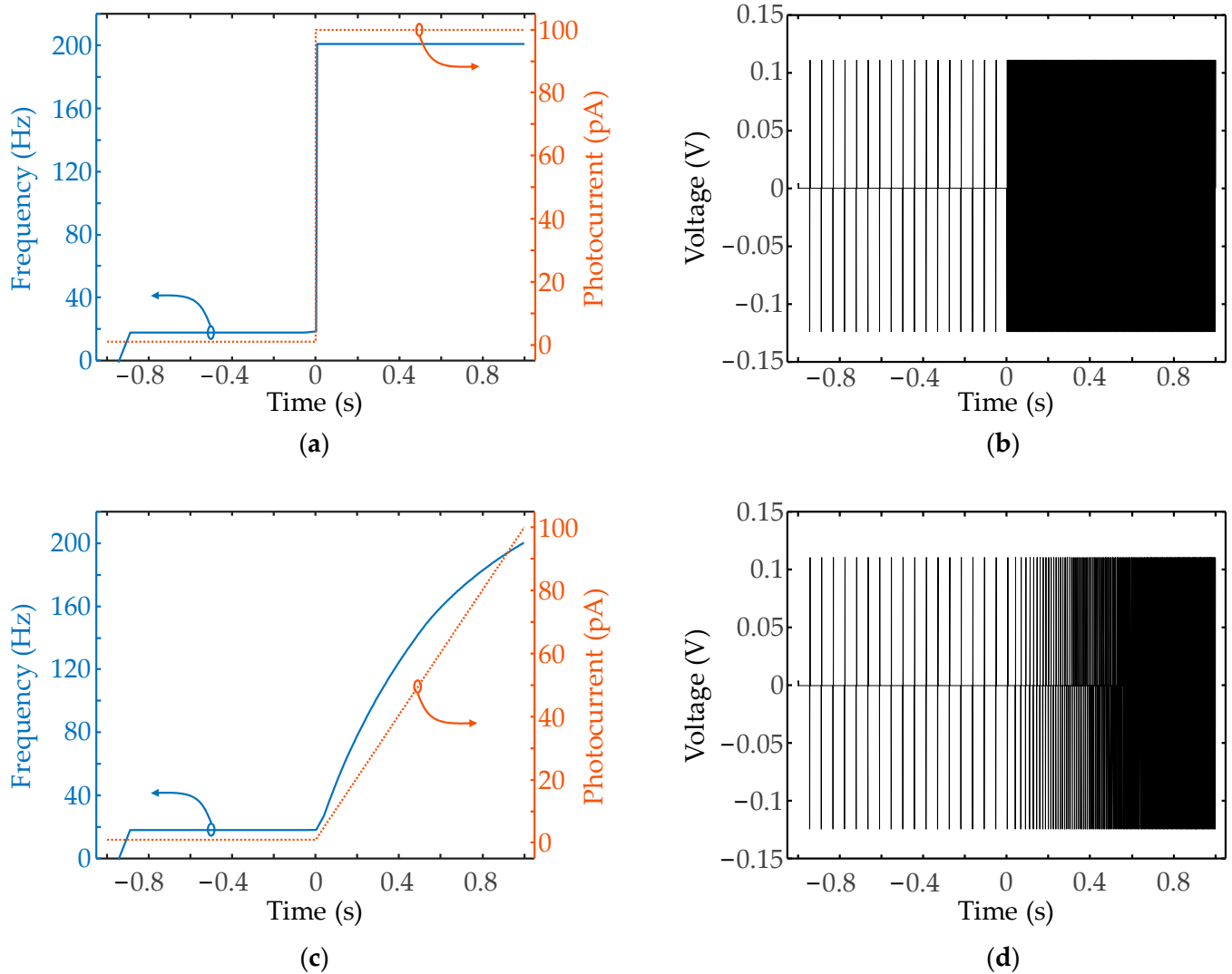


Figure 13. Simulation results of stimulus trigger generator: (a) Circuit response with photocurrent step; (b) Biphasic current waveform of step response; (c) Circuit response with photocurrent ramp; (d) Biphasic current waveform of ramp response.

Due to the unavoidable process variation, the frequency of biphasic current can vary from wafer to wafer or lot to lot. Figure 14a,b show the Monte Carlo simulation of the proposed circuit. As a reference, the red lines indicate the measured results. Process variation can change the threshold of transistors. An elaborately designed layout can minimize the mismatch. Furthermore, the transistors in digital parts act as switches; they are robust to process variation.

The most variation-vulnerable component in the circuit is the capacitor, which has good matching characteristics but whose absolute value is greatly affected by manufacturing. As described in Equations (1)–(5), the capacitors C_A , C_B , and C_C determine the PRF and pulse width of biphasic current. With a well-designed layout, the cathodic and anodic pulse widths still well match each other, maintaining the charge balance. On the other hand, the PRF of stimulus current varies between 4~34 Hz with 1 pA photocurrent

and 46~276 Hz with 100 pA photocurrent. It means that trimming is necessary, and it can be done through the configuration of the current source I_A , I_B , and I_C in the STG.

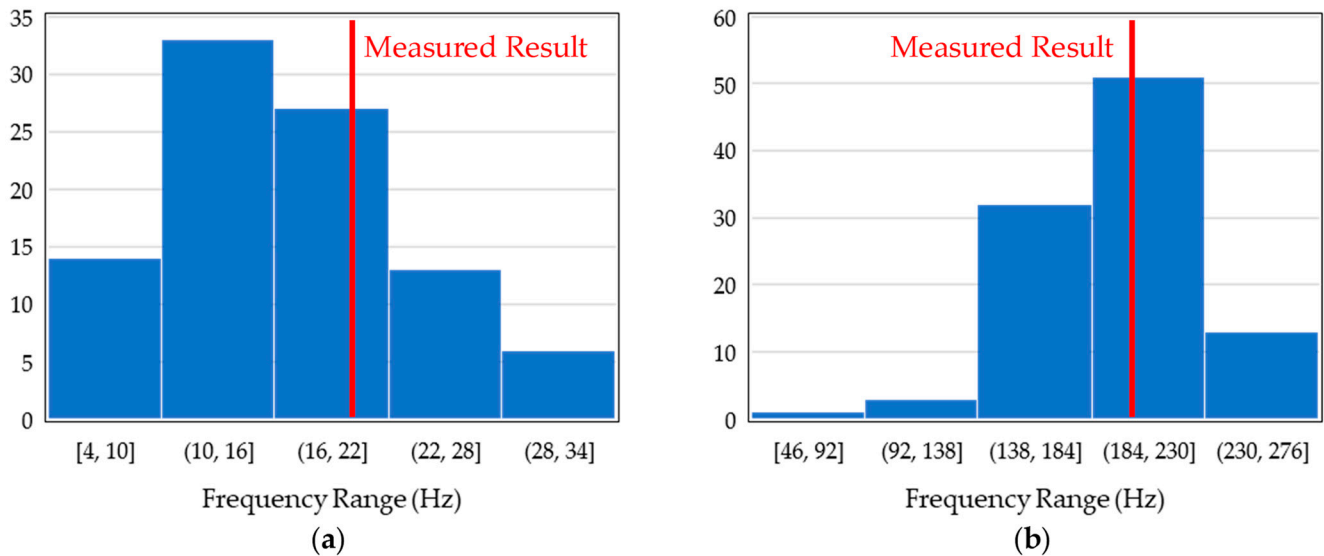


Figure 14. Monte Carlo simulation results: (a) Frequency variation of biphasic current when photocurrent = 1 pA; (b) Frequency variation of biphasic current when photocurrent = 100 pA.

Next, the FVP circuit is enabled for functional verification. The photocurrent is swept from 1 pA to 100 pA with ten steps per decade. The flicker fusion threshold is set to 10 pA (corresponding to a PRF of about 50 Hz). As shown in Figure 15, when the current is lower than 10 pA, the frequency of VCT_{STG} and VAT_{STG} pulses is below the flicker fusion threshold, and the FVP circuit blocks the stimulus current. Therefore, no current pulse occurs on the output of BCS, as marked by the circle.

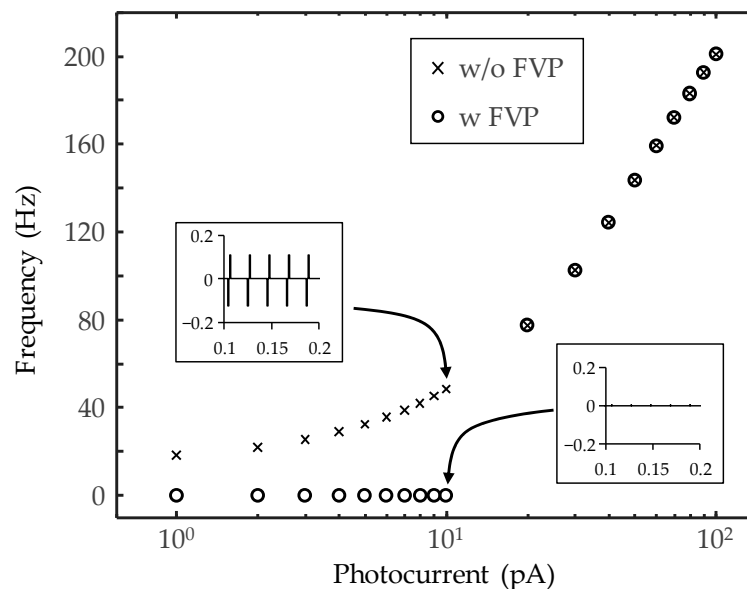


Figure 15. Simulation results of flicker vision prevention (FVP) circuit.

With a larger input current, the pulse width of DIS_{STG} becomes short enough. As shown in Figure 10, the accumulated voltage on the capacitor will not cross the threshold of the latch; the EN signal is always high. The FVP circuit allows VCT_{STG} and VAT_{STG} signals to pass through. The BCS generates the current pulse as usual.

To verify the E- μ Saccade function, a circuit prototype is fabricated in a 0.18 μm standard CMOS process. Table 2 summarizes the design information. Figure 16a–c show the micrograph of the E- μ Saccade circuit. As shown in Figure 16d, a probe card is used to apply the necessary signals to the fabricated chip and read the biphasic stimulus current, and a light source is used to provide the test light pattern to the circuit. The CBMUX array is designed as a 3×3 array, the minimum required pixel number to perform microsaccade operation for conducting microsaccade operation. To maximize the illumination difference for better output observation, the four SCG are maximally separated. The distance between them is about 700 μm .

Table 2. Summary of design information.

Process	0.18 μm Standard CMOS 1P6M
Power Supply	1.8 V
Pixel Count	3×3
STG Pixel Size	$75 \times 75 \mu\text{m}^2$ (Including FVP circuit)
CBMUX Pixel Size	$45 \times 26 \mu\text{m}^2$
Power Consumption	$8.255 \mu\text{W}/\text{pixel}$ @PRF = 100 Hz
Microsaccade Speed	0.1 or 1 Hz
External Component	Decoupling Capacitors

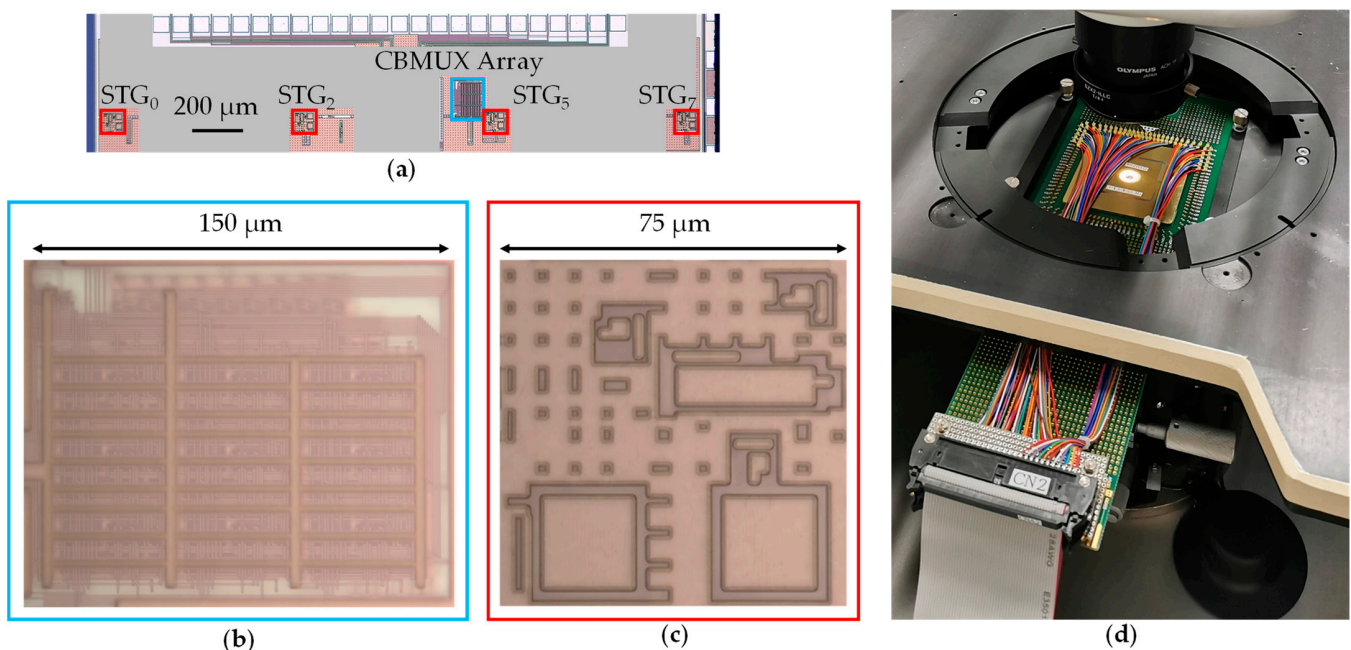


Figure 16. Measurement setup: (a) Micrograph of the fabricated prototype; (b) Micrograph of the CBMUX array; (c) Micrograph of the STG; (d) The probe card and light source for circuit function verification.

The block diagram of the measurement setup is shown in Figure 17. Four STG are configured to sense ambient light (corresponding to the PSC of 0, 2, 5, and 7). A signal generator is used for directly feeding frequency-controllable VCT and VAT signals to the rest of the input terminals of CBMUX (corresponding to the PSC of 1, 3, 4, 6, and 8). The center BCS is connected to an oscilloscope for monitoring the stimulus current waveform. Thus, the biphasic current with different frequencies can be observed on the oscilloscope by sending the proper value of PSC to CBMUX.

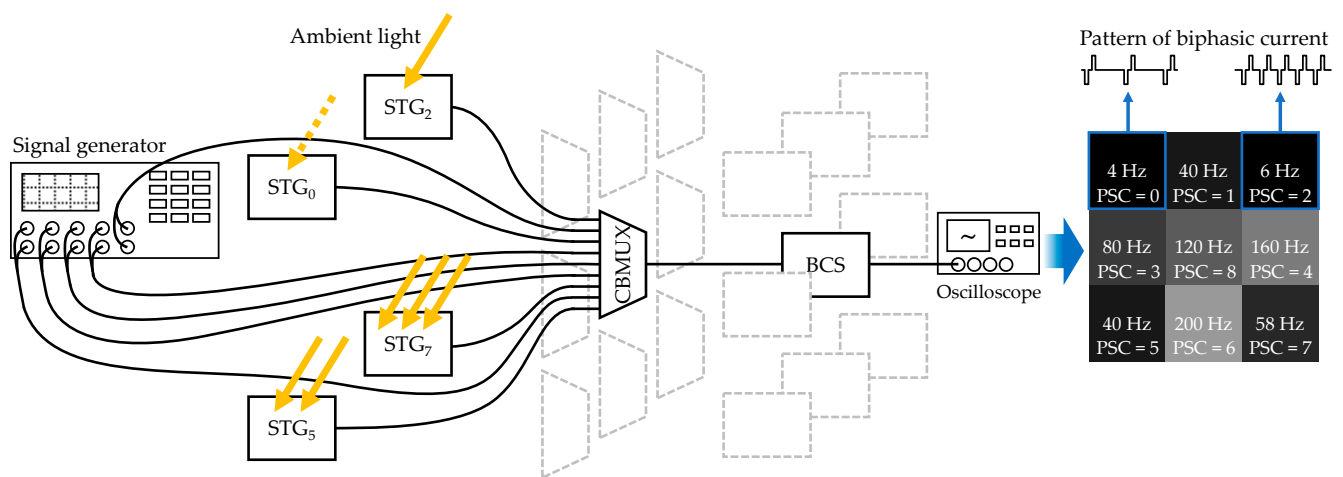


Figure 17. Block diagram of the measurement setup.

A PSC of 4 sets the CBMUX to connect the STG₄ running at 160 Hz to the BCS connected to an oscilloscope. Therefore, a biphasic current of 160 Hz can be observed, as shown in Figure 18. Although in practice, the stimulus current is tens of μA not to hurt the retina cell. This test sets the stimulus current to a higher level for better observation. With the fabrication process and the designed transistor size, the maximum output current is about $80 \mu\text{A}$, which is translated into $\pm 0.8 \text{ V}$ by the $10 \text{ k}\Omega$ tissue load resistor. To verify dynamic microsaccade operation, PSC is varied every 100 ms (10 Hz) and 1 s (1 Hz), and the CBMUX changes the signal path from different STGs to the center BCS.

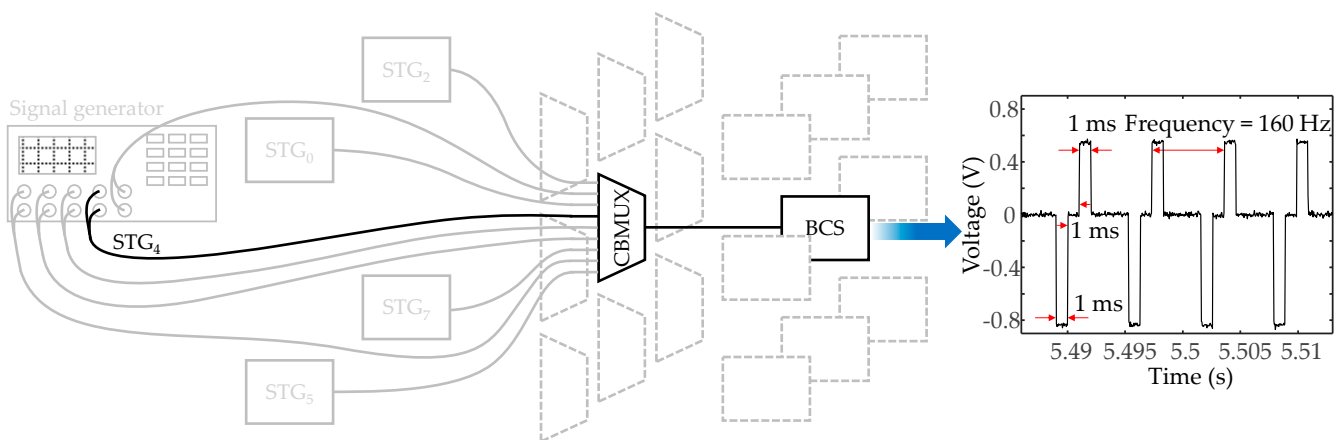


Figure 18. Measured waveform of biphasic current when PSC = 4.

The frequency variation of biphasic current during microsaccade operation is shown in Figure 19. First, the frequency of CLK_{MS} is set to 1 Hz. When fed by a PSC sequence of $\{0, 1, 2, 3, 4, 5, 6, 7, 8, 9\}$, the frequency of the biphasic current of the center BCS varies in the order of $\{4 \text{ Hz}, 40 \text{ Hz}, 6 \text{ Hz}, 80 \text{ Hz}, 160 \text{ Hz}, 40 \text{ Hz}, 200 \text{ Hz}, 58 \text{ Hz}, \text{ and } 120 \text{ Hz}\}$, and then returns to 4 Hz again. The frequency of stimulus current is stable during the silent phase of the microsaccade, which is expected to provide a more stable visual perception.

Due to the high operation speed of pattern movement, only several stable pulses can be sent out in a short microsaccade period (0.1 s) when the PRF of the stimulus current is as low as tens of Hz. When the CLK_{MS} is increased to 10 Hz and a PSC sequence of $\{1, 3, 4, 6, \text{ and } 8\}$ is fed to the circuit, the frequency drop that comes from signal switching is no longer negligible. Details about the frequency drop are in Section 4.

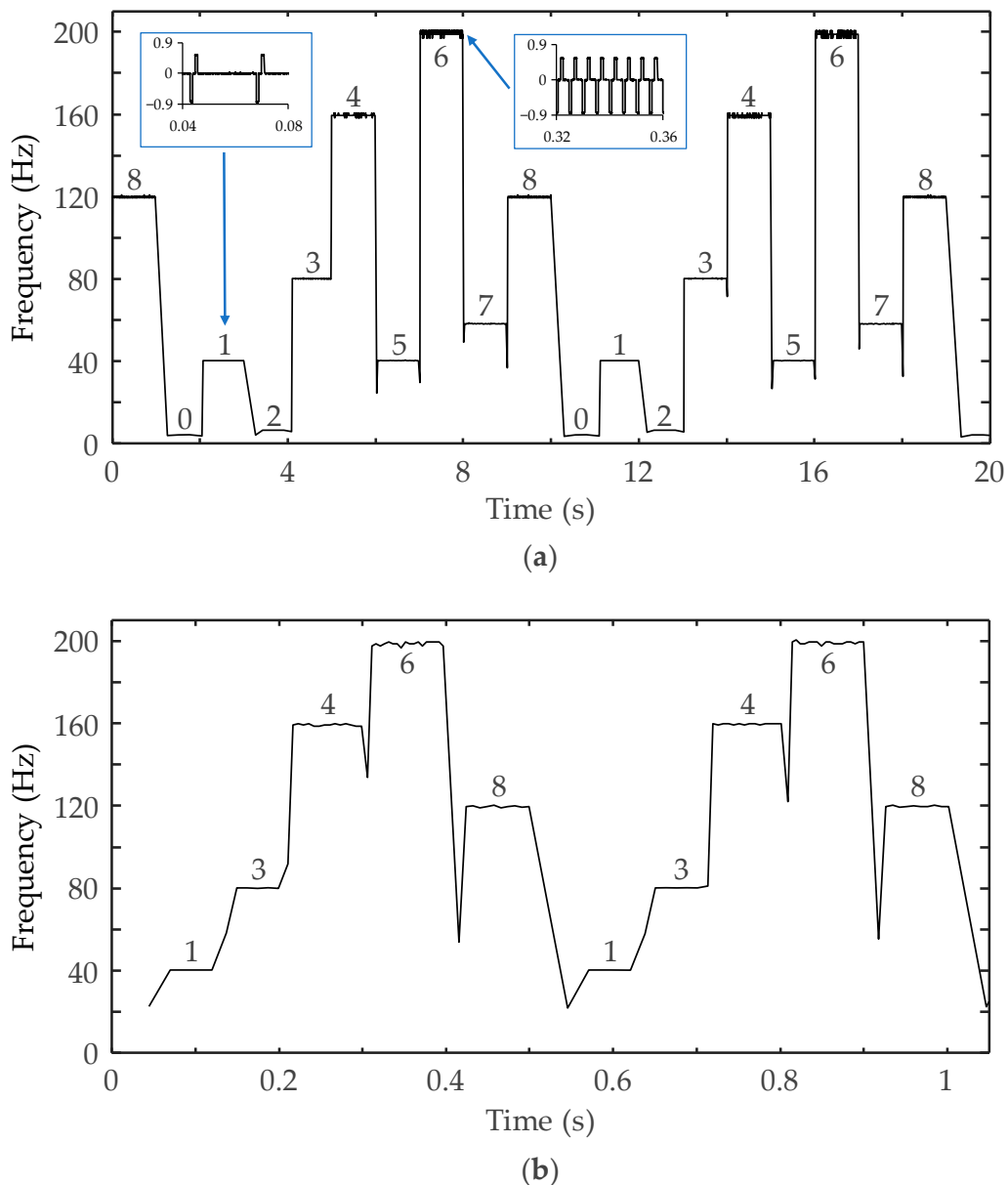


Figure 19. Measured results of the proposed E- μ Saccade circuit: (a) Microsaccade operates at 1 Hz; (b) Microsaccade operates at 10 Hz.

4. Discussion

The main function of the proposed circuit relies on VAT and VCT signals. Therefore, any improper waveform, such as a glitch, can lead to the malfunction of the circuit. In the STG shown in Figure 7, QN must be reset to 1 only when the output of the Schmitt trigger falls to the ground. If not, a glitch can be generated on the VCT signal line. Although a narrow pulse of several tens of nanoseconds would not affect the neurons' charge balance, the timing chart of the proposed circuit could break down. Therefore, an additional delay must be considered at the R terminal of the latch.

The artificial eyeball system must satisfy the need for low power consumption. In the FVP circuit shown in Figure 8, given a slow-varying stimulus trigger signal, the dynamic current of the RS latch can be too large to prevent normal operation. Therefore, an inverter with a large L/W ratio is added to the R terminal of the latch to avoid excessive dynamic current and introduce an extra delay for correct operation.

In Figure 13c, the conversion gain degenerates when the photocurrent is high. The reason for the results is that the portion of the stimulation period ($T_{VCT} + T_{VAT} + T_{GAP} = 3$ ms) is small at low frequency, and the DIS signal dominates the PRF of the stimulus current. As the biphasic current goes faster, the DIS phase, the variable portion, also becomes shorter. Finally, the PRF will converge to the theoretical limit of 333 Hz ($T_{VCT} = T_{VAT} = T_{GAP} = 1$ ms).

For stable visual perception, a slow microsaccade operation is desired. If the operation speed of the microsaccade is too fast, the vision nerve cannot receive enough pulses to generate perception. The results shown in Figure 19a,b indicate that if allowed in clinical usage, the microsaccade operation should be in the range of seconds, and they match the finding in [30] well that high-frequency eye movement is detrimental to visual perception.

In our previous work, the vision fading problem in vision restoration was found and addressed. However, the artificial eyeball still suffers from flickering vision problems. There is no current work that focuses on the issue. This work proposed and added the flicker vision prevention circuit to the microsaccade circuit, making it the first practical artificial vision system.

In the future, to build a fully functional artificial eyeball system, all the verified building blocks in this work will be expanded into a full array with 32 by 32 pixels for achieving simple pattern recognition. For solving the mismatch problem, binary stimulation instead of continuous stimulation can be adopted, which means that only pixels with brightness over the threshold are allowed to send out stimulation current. To connect the proposed artificial eye circuit to the visual neuron, a cuffless electrode that surrounds the optic nerve or a Utah array that deepens into brain tissue can be considered.

5. Conclusions

The artificial eyeball is becoming a promising treatment for every blindness, which replaces the biological eye and restores vision for virtually all blindness. In the human eye, microsaccade is critical to avoiding vision fading. This study is the first to focus on mimicking microsaccades in the biological eye. In addition, the flickering vision comes from low-frequency stimulus current, and charge imbalance issues are also considered.

A 3×3 circuit prototype is designed and fabricated for function verification in the TSMC 0.18 μm CMOS process. In the future, the simulation results will show that the light-to-frequency ratio correctly tracks the ambient light change and that the FVP circuit stops the stimulation in low illuminance conditions. The measurement results show that the circuit can move the image in eight directions at the frequency given by the global clock. Furthermore, pre-defined commands define the direction of the movement. The stimulus current waveform shows that no pulse mismatch occurs. With the proposed E- μ Saccade circuit, the vision fading issue can be alleviated, and the more visually impaired can benefit from the artificial eyeball system.

Author Contributions: Conceptualization, Y.L., B.D. and T.T.; methodology, Y.L., K.N. and B.D.; validation, Y.L., S.W., B.I. and Y.A.; formal analysis, Y.L.; investigation, Y.L. and K.N.; resources, H.K., T.F. and K.K.; writing—original draft preparation, Y.L.; writing—review and editing, Y.L. and T.T.; supervision, T.T.; funding acquisition, T.T. All authors have read and agreed to the published version of the manuscript.

Funding: This work was partly funded by JSPS KAKENHI Grant Number 21H04951.

Data Availability Statement: Not applicable.

Acknowledgments: This work was supported by JSPS KAKENHI Grant Number 21H04951. This work was also supported through the activities of VDEC, The University of Tokyo, in collaboration with Cadence Design Systems and Siemens Electronic Design Automation Japan K.K. Y.L. appreciates the financial support from the China Scholarship Council (Grant Number: 201806380013).

Conflicts of Interest: The authors declare no conflict of interest.

References

1. Bourne, R.; Steinmetz, J.D.; Flaxman, S.; Briant, P.S.; Taylor, H.R.; Resnikoff, S.; Casson, R.J.; Abdoli, A.; Abu-Gharbieh, E.; Afshin, A.; et al. Trends in Prevalence of Blindness and Distance and near Vision Impairment over 30 Years: An Analysis for the Global Burden of Disease Study. *Lancet Glob. Health* **2021**, *9*, e130–e143. [\[CrossRef\]](#)
2. Zrenner, E. Fighting Blindness with Microelectronics. *Sci. Transl. Med.* **2013**, *5*, 210ps16. [\[CrossRef\]](#)
3. Weiland, J.D.; Humayun, M.S. Retinal Prosthesis. *IEEE Trans. Biomed. Eng.* **2014**, *61*, 1412–1424. [\[CrossRef\]](#)
4. Ong, J.M.; da Cruz, L. The Bionic Eye: A Review. *Clin. Experiment. Ophthalmol.* **2012**, *40*, 6–17. [\[CrossRef\]](#)
5. Chuang, A.T.; Margo, C.E.; Greenberg, P.B. Retinal Implants: A Systematic Review. *Br. J. Ophthalmol.* **2014**, *98*, 852–856. [\[CrossRef\]](#)
6. Hammes, H.-P.; Feng, Y.; Pfister, F.; Brownlee, M. Diabetic Retinopathy: Targeting Vasoregression. *Diabetes* **2011**, *60*, 9–16. [\[CrossRef\]](#)
7. El-Danaf, R.N.; Huberman, A.D. Characteristic Patterns of Dendritic Remodeling in Early-Stage Glaucoma: Evidence from Genetically Identified Retinal Ganglion Cell Types. *J. Neurosci.* **2015**, *35*, 2329–2343. [\[CrossRef\]](#) [\[PubMed\]](#)
8. Gu, L.; Poddar, S.; Lin, Y.; Long, Z.; Zhang, D.; Zhang, Q.; Shu, L.; Qiu, X.; Kam, M.; Javey, A.; et al. A Biomimetic Eye with a Hemispherical Perovskite Nanowire Array Retina. *Nature* **2020**, *581*, 278–282. [\[CrossRef\]](#)
9. Dobbelle, W.H. Artificial Vision for the Blind by Connecting a Television Camera to the Visual Cortex. *ASAIO J.* **2000**, *46*, 3–9. [\[CrossRef\]](#)
10. Rush, A.D.; Troyk, P.R. A Power and Data Link for a Wireless-Implanted Neural Recording System. *IEEE Trans. Biomed. Eng.* **2012**, *59*, 3255–3262. [\[CrossRef\]](#)
11. Tomioka, K.; Toyoda, K.; Ishizaki, T.; Noda, T.; Ohta, J.; Kimura, M. Retinal Prosthesis Using Thin-Film Devices on a Transparent Substrate and Wireless Power Transfer. *IEEE Trans. Electron. Devices* **2020**, *67*, 529–534. [\[CrossRef\]](#)
12. Wu, C.-Y.; Tseng, C.-K.; Liao, J.-H.; Chiao, C.-C.; Chu, F.-L.; Tsai, Y.-C.; Ohta, J.; Noda, T. CMOS 256-Pixel/480-Pixel Photovoltaic-Powered Subretinal Prosthetic Chips with Wide Image Dynamic Range and Bi/Four-Directional Sharing Electrodes and Their Ex Vivo Experimental Validations with Mice. *IEEE Trans. Circuits Syst. Regul. Pap.* **2020**, *67*, 3273–3283. [\[CrossRef\]](#)
13. Lemaire, W.; Benhouria, M.; Koua, K.; Besrou, M.; Gauthier, L.-P.; Martin-Hardy, G.; Rossignol, T.; Roy, S.; Fontaine, R. Retinal Stimulator ASIC Architecture Based on a Joint Power and Data Optical Link. *IEEE J. Solid-State Circuits* **2021**, *56*, 2158–2170. [\[CrossRef\]](#)
14. Kelly, S.K.; Shire, D.B.; Chen, J.; Doyle, P.; Gingerich, M.D.; Cogan, S.F.; Drohan, W.A.; Behan, S.; Theogarajan, L.; Wyatt, J.L.; et al. A Hermetic Wireless Subretinal Neurostimulator for Vision Prostheses. *IEEE Trans. Biomed. Eng.* **2011**, *58*, 3197–3205. [\[CrossRef\]](#)
15. Martinez-Conde, S.; Macknik, S.L.; Hubel, D.H. The Role of Fixational Eye Movements in Visual Perception. *Nat. Rev. Neurosci.* **2004**, *5*, 229–240. [\[CrossRef\]](#)
16. Hamed, Z.M.; Goffart, L.; Krauzlis, R.J. A Neural Mechanism for Microsaccade Generation in the Primate Superior Colliculus. *Science* **2009**, *323*, 940–943. [\[CrossRef\]](#)
17. Dimigen, O.; Valsecchi, M.; Sommer, W.; Kliegl, R. Human Microsaccade-Related Visual Brain Responses. *J. Neurosci.* **2009**, *29*, 12321–12331. [\[CrossRef\]](#)
18. Collewijn, H.; Kowler, E. The Significance of Microsaccades for Vision and Oculomotor Control. *J. Vis.* **2008**, *8*, 20. [\[CrossRef\]](#)
19. Kowler, E. Eye Movements: The Past 25years. *Vision Res.* **2011**, *51*, 1457–1483. [\[CrossRef\]](#)
20. Stronks, H.C.; Dagnelie, G. The Functional Performance of the Argus II Retinal Prosthesis. *Expert Rev. Med. Devices* **2014**, *11*, 23–30. [\[CrossRef\]](#)
21. Singh, P.R.; Liu, W.; Sivaprakasam, M.; Humayun, M.S.; Weiland, J.D. A Matched Biphasic Microstimulator for an Implantable Retinal Prosthetic Device. In Proceedings of the 2004 IEEE International Symposium on Circuits and Systems (ISCAS), Vancouver, BC, Canada, 23–26 May 2004; Volume 4, p. IV–1.
22. Sivaprakasam, M.; Liu, W.; Humayun, M.S.; Weiland, J.D. A Variable Range Bi-Phasic Current Stimulus Driver Circuitry for an Implantable Retinal Prosthetic Device. *IEEE J. Solid-State Circuits* **2005**, *40*, 763–771. [\[CrossRef\]](#)
23. Sivaprakasam, M.; Liu, W.; Wang, G.; Weiland, J.D.; Humayun, M.S. Architecture Tradeoffs in High-Density Microstimulators for Retinal Prosthesis. *IEEE Trans. Circuits Syst. Regul. Pap.* **2005**, *52*, 2629–2641. [\[CrossRef\]](#)
24. Palanker, D.; Le Mer, Y.; Mohand-Said, S.; Muqit, M.; Sahel, J.A. Photovoltaic Restoration of Central Vision in Atrophic Age-Related Macular Degeneration. *Ophthalmology* **2020**, *127*, 1097–1104. [\[CrossRef\]](#)
25. Liu, W.; Humayun, M.S. Retinal Prosthesis. In Proceedings of the 2004 IEEE International Solid-State Circuits Conference (IEEE Cat. No.04CH37519), San Francisco, CA, USA, 15–19 February 2004; Volume 1, pp. 218–219.
26. Horsager, A.; Greenberg, R.J.; Fine, I. Spatiotemporal Interactions in Retinal Prosthesis Subjects. *Investig. Ophthalmol. Vis. Sci.* **2010**, *51*, 1223–1233. [\[CrossRef\]](#)
27. Eisen-Enosh, A.; Farah, N.; Burgansky-Eliash, Z.; Polat, U.; Mandel, Y. Evaluation of Critical Flicker-Fusion Frequency Measurement Methods for the Investigation of Visual Temporal Resolution. *Sci. Rep.* **2017**, *7*, 15621. [\[CrossRef\]](#)
28. Shimokawa, K.; Qian, Z.; Takezawa, Y.; Kino, H.; Fukushima, T.; Kiyoyama, K.; Tanaka, T. Experimental Evaluation of Stimulus Current Generator with Laplacian Edge-Enhancement for 3-D Stacked Retinal Prosthesis Chip. In Proceedings of the 2017 IEEE Biomedical Circuits and Systems Conference (BioCAS), Turin, Italy, 19–21 October 2017; pp. 1–4.
29. Liang, Y.; Qian, Z.; Du, B.; Ye, J.; Nakamura, K.; Wang, S.; Kino, H.; Fukushima, T.; Kiyoyama, K.; Tanaka, T. Design and Evaluation of Electronic-Microsaccade with Balanced Stimulation for Artificial Vision System. In Proceedings of the 2021 IEEE Biomedical Circuits and Systems Conference (BioCAS), Berlin, Germany, 7–9 October 2021; pp. 01–04.

30. Martinez-Conde, S.; Macknik, S.L.; Troncoso, X.G.; Dyar, T.A. Microsaccades Counteract Visual Fading during Fixation. *Neuron* **2006**, *49*, 297–305. [[CrossRef](#)]
31. Rolfs, M. Microsaccades: Small Steps on a Long Way. *Vision Res.* **2009**, *49*, 2415–2441. [[CrossRef](#)]
32. Naganuma, H.; Kiyoyama, K.; Tanaka, T. A 37×37 Pixels Artificial Retina Chip with Edge Enhancement Function for 3-D Stacked Fully Implantable Retinal Prosthesis. In Proceedings of the 2012 IEEE Biomedical Circuits and Systems Conference (BioCAS), Hsinchu, Taiwan, 28–30 November 2012; pp. 212–215.
33. Bekerman, I.; Gottlieb, P.; Vaiman, M. Variations in Eyeball Diameters of the Healthy Adults. *J. Ophthalmol.* **2014**, *2014*, 503645. [[CrossRef](#)]
34. Pérez Fornos, A.; Sommerhalder, J.; da Cruz, L.; Sahel, J.A.; Mohand-Said, S.; Hafezi, F.; Pelizzone, M. Temporal Properties of Visual Perception on Electrical Stimulation of the Retina. *Investig. Ophthalmol. Vis. Sci.* **2012**, *53*, 2720–2731. [[CrossRef](#)]
35. Asher, A.; Segal, W.A.; Baccus, S.A.; Yaroslavsky, L.P.; Palanker, D.V. Image Processing for a High-Resolution Optoelectronic Retinal Prosthesis. *IEEE Trans. Biomed. Eng.* **2007**, *54*, 993–1004. [[CrossRef](#)]
36. Weitz, A.C.; Behrend, M.R.; Ahuja, A.K.; Christopher, P.; Wei, J.; Wuyyuru, V.; Patel, U.; Greenberg, R.J.; Humayun, M.S.; Chow, R.H.; et al. Interphase Gap as a Means to Reduce Electrical Stimulation Thresholds for Epiretinal Prostheses. *J. Neural Eng.* **2014**, *11*, 016007. [[CrossRef](#)]
37. Carlyon, R.P.; van Wieringen, A.; Deeks, J.M.; Long, C.J.; Lyzenga, J.; Wouters, J. Effect of Inter-Phase Gap on the Sensitivity of Cochlear Implant Users to Electrical Stimulation. *Hear. Res.* **2005**, *205*, 210–224. [[CrossRef](#)]
38. John, S.E.; Shivdasani, M.N.; Williams, C.E.; Morley, J.W.; Shepherd, R.K.; Rathbone, G.D.; Fallon, J.B. Suprachoroidal Electrical Stimulation: Effects of Stimulus Pulse Parameters on Visual Cortical Responses. *J. Neural Eng.* **2013**, *10*, 056011. [[CrossRef](#)]

Disclaimer/Publisher’s Note: The statements, opinions and data contained in all publications are solely those of the individual author(s) and contributor(s) and not of MDPI and/or the editor(s). MDPI and/or the editor(s) disclaim responsibility for any injury to people or property resulting from any ideas, methods, instructions or products referred to in the content.